

Low-cycle fatigue performance of remelted laser powder bed fusion (L-PBF) biomedical Ti25Ta

Erin G. Brodie ^{a,b,*}, Julia Richter ^d, Thomas Wegener ^d, Thomas Niendorf ^d, Andrey Molotnikov ^{a,b,c,**}

^a Department of Materials Science and Engineering, Monash University, Clayton, VIC, 3800, Australia

^b Monash Centre for Additive Manufacturing (MCAM), 11 Normanby Road, Nottinghill, VIC, 3168, Australia

^c RMIT Centre for Additive Manufacturing, School of Engineering, RMIT University, Melbourne, Australia

^d University of Kassel, Institute of Materials Engineering – Metallic Materials, Moenchebergstrasse 3, 34125, Kassel, Germany



ARTICLE INFO

Keywords:

Tantalum
Titanium
Laser powder bed fusion
Low-cycle fatigue

ABSTRACT

In this study, the fatigue performance of additively manufactured Ti25Ta, produced by laser powder bed fusion (L-PBF) using pre-mixed powder is investigated. Ti25Ta shows promise as a biomedical implant alloy, due to its high strength to elastic modulus ratio. However, the fatigue response of L-PBF Ti25Ta is yet unknown and understanding fatigue behaviour is crucial for cyclically loaded implants.

The Ti25Ta alloy was produced employing single melt and remelt scanning strategies. It was shown that the remelt strategy had a positive effect on reducing the amount of remaining partially melted Ta particles from 2.07 ± 0.01 vol % to 0.22 ± 0.01 vol % while only slightly increasing the porosity from 0.15 ± 0.01 vol % to 0.37 ± 0.01 vol %. Furthermore, it was found that the remelt strategy resulted in alloy strengthening and a randomised orientation of the α' lath microstructure.

Machined fatigue samples were tested in the low-cycle fatigue regime under strain-controlled conditions. The alloy demonstrated a superior yield stress normalised fatigue performance compared with commercially pure (CP) Ti, and Ti-6Al-4V ELI, and was second only to pure Ta. However, the Ti25Ta L-PBF material retains less than half the elastic modulus of all the compared materials. The remelt samples showed an increased stress response due to their higher strength and an increased elastic modulus, however a reduced number of cycles to failure. This was attributed to reduced ductility and increased crack propagation rate. It is believed that remelt scan parameter optimisation can further enhance the performance of this alloy.

1. Introduction

The orthopaedics industry is integrating additive manufacturing (AM) into their business due to the advantages of personalised implants and improved functionality. Among several AM techniques, laser powder bed fusion (L-PBF) is a dominant method of implant manufacture, providing the ability to create parts which mimic body structures and include complex geometries, such as lattices [1]. Ti-6Al-4V, the most common biomedical alloy, has been widely investigated in L-PBF studies. Studies investigating the fatigue properties of L-PBF Ti-6Al-4V, critical for applications of cyclically loaded implants, highlight the detrimental effects of residual stress and process-induced porosity on fatigue life [2–8]. Furthermore, crack initiation is shown to be

dependent on microstructure [9–12] and surface roughness of ‘as-built’ parts can severely reduce fatigue life [8,13–15]. However, higher implant surface roughness has a positive effect on the biological response. Rougher surfaces tend to cause better bone cell attachment and hence higher implant stability [16–18]. Therefore, a balance must be found between good biological response and the mechanical requirements of the implant.

Both mechanical and chemical changes to the current Ti-6Al-4V alloy can benefit implant integration with the body. For example, the effects of ‘stress-shielding’ and bone resorption can be reduced by implant materials with an elastic modulus similar to bone (5–30 GPa) [19,20]. Ti-6Al-4V has an elastic modulus of 113 GPa, however new β -Ti alloys display a reduced elastic modulus, due to β phase stabilising

* Corresponding author. Monash Centre for Additive Manufacturing (MCAM), 11 Normanby Road, Nottinghill, VIC, 3168, Australia.

** Corresponding author. RMIT Centre for Additive Manufacturing, School of Engineering, RMIT University, Melbourne, Australia.

E-mail addresses: erin.brodie@monash.edu (E.G. Brodie), andrey.molotnikov@rmit.edu.au (A. Molotnikov).

elements such as Nb, Zr, Mo and Ta. The Ti–Nb–Ta–Zr (TNTZ) alloy can achieve a modulus very similar to that of bone, 35 GPa, however, only as a single crystal [21]. In polycrystalline form, the TNTZ alloy when cold rolled returns a much higher elastic modulus range from 60 to 100 GPa [22]. Single crystal processing is unsuitable for implant manufacture, and hence further materials and manufacturing methods must be considered.

Further β -Ti alloys, such as Ti–Nb, Ti–Nb–Zr, Ti–Nb–Zr–Ta and Ti–Nb–Zr–Sn, show a reduced elastic modulus of 60–80 GPa [22]. However, the static and fatigue strengths of these low modulus β -Ti alloys often require improvements to be suitable for implant applications [23]. Strengthening can be achieved by severe cold working, ceramic additives and solid solution strengthening, typically with oxygen [24]. However, these conventional strengthening mechanisms are often coupled with reduced alloy ductility, detrimental to fatigue performance. When manufactured by L-PBF, these alloys show elastic modulus and strength values within the range of the conventionally produced alloys [25–29] (see Table 1), however only few studies have investigated their fatigue response. One promising study of L-PBF Ti–Nb–Zr–Sn revealed a higher normalised fatigue strength than L-PBF Ti–6Al–4V, due to its super-elasticity and ability to form a larger plastic zone ahead of the fatigue crack tip [30]. The alloy density was manipulated using lattice structures to show that an equal fatigue strength to Ti–6Al–4V could be obtained, whilst retaining only half the elastic modulus.

The Ti–Ta alloy system shows promise as a bone implant alloy, not only due to its low elastic modulus [31] but also due to the chemical nature of Ta which has shown to cause superior osseointegration [32–34]. The Ti25 wt% Ta alloy possesses a similar strength to pure titanium, however, with a much lower elastic modulus [35]. Preliminary porous structures for load bearing implants have been manufactured by L-PBF in both Ti25 wt% Ta [36] and Ti30 wt% Ta [37] compositions however, the fatigue response of this alloy system has been little investigated. The fatigue performance of the Ti30 wt% Ta porous structure was compared with identical porous structures in pure Ta, pure Ti, Ti–6Al–4V, and whilst pure Ta showed the highest relative fatigue strength, attributed to its high ductility and β -phase structure [32,38], the Ti30 wt% Ta alloy showed the highest fatigue strength for its stiffness [37]. The fatigue response of the L-PBF Ti25 wt% Ta alloy has not been investigated, nor have any L-PBF TiTa compositions in solid form. The Ti25 wt% Ta alloy may also show a significant difference in mechanical behaviour to the Ti30 wt% Ta alloy, despite their similar composition. A phase boundary between α'/α'' exists between these two compositions and is still disputed in literature [31,39–42].

The promising new β -Ti alloys, however, pose difficulties for L-PBF processing, due to the refractory nature of the β stabilising elements. Moreover, only few exist in pre-alloyed form. Instead, elemental metal powders are mixed to create the powder feed stock which can result in material inhomogeneity [25,35,43,44]. One strategy which may reduce inhomogeneity is a remelt scanning strategy. Remelt scanning involves two or more passes of the laser over the melted surface area for each powder layer. Several studies report its use to alter the density, surface quality, microstructure and residual stress of L-PBF parts [45–57], however not as a homogenisation tool. These studies observe that the remelt scanning strategy can increase part density [45–48,55,57] and

improve surface quality [49–51], by inducing a second stage of molten flow which fills pre-existing defects. In addition, the remelt scan results in finer grain structures [47,52,53] and can alter the part residual stress [45,54]. No research has yet been conducted investigating the fatigue properties of material produced using a remelt scan strategy.

In this study, Ti25Ta was produced via L-PBF using both a single scan and remelt scan strategy. All alloy compositions are referred to henceforth in wt%. The material microstructure was characterised using electron back scattered diffraction (EBSD) and the porosity and homogeneity were investigated using X-ray computed tomography (Micro-CT). Fatigue samples were tested in the low-cycle fatigue (LCF) regime, covering the transition between plastic and elastic deformation regions, to determine the number of cycles to failure. Whilst plastic strain is undesired in final implant applications, understanding when cyclic softening may occur is essential for full deformation characterisation of the material. Fractography and electron dispersive X-ray (EDX) analysis was used to support the mechanical observations and elucidate the effect of the material composition on the fatigue behaviour. Finally, the fatigue behaviour is compared with L-PBF pure Ta, commercially pure (CP) Ti and Ti–6Al–4V to determine its suitability for implant applications.

2. Materials and methods

2.1. Sample fabrication and microstructure analysis

Fatigue samples were produced from pre-mixed Ti25Ta spherical powders, characterised by a particle diameter range from 15 to 45 μm . A Concept Laser Mlab Cusing R machine was used and samples were printed under an argon atmosphere, with the parameters in Table 2. A 90° rotation of the scanning pattern was applied between consecutive layers. A second pass of the laser was applied per layer to create the ‘remelt’ scanning condition. The remelt scan used the same parameters listed in Table 2 and followed the identical scanning path to the first laser scan. Optimisation of the single melt and remelt parameters are presented in Ref. [35].

Sample blocks of 12 mm (x) \times 22 mm (y) \times 31 mm (z) were printed and flat samples were electro-discharge machined (EDM) from the centre of the block to the dimensions shown in Fig. 1b. Only one build orientation was considered due to equiaxed grain structure observed in Ref. [35]. All sample blocks were printed in the same build job to avoid variance between builds. For mechanical testing, the sample surfaces were prepared by grinding to P1200 grit size and loaded in the building direction (z).

The grip sections (y-z plane) of the tested samples were prepared for EBSD analysis by mechanical grinding and polishing followed by two

Table 2
Printing parameters.

L-PBF process parameter	Value
Laser Power, P	95 W
Scan Speed, v	300 mm/s
Hatch distance, h	35 μm
Layer thickness, t	25 μm

Table 1

Summary of mechanical properties of conventional and AM β -Ti alloys.

AM Method	Elastic Modulus (GPa)	Ultimate Tensile Strength (MPa)	Elongation at fracture (%)	Reference
Ti–Nb (26–45 wt %)	Conventional	50–99	420–865	[58–60]
Ti–Ta (10–80 wt %)	Conventional	67–100	500–700	[61]
Ti–Nb (26–45 wt %)	L-PBF/L-DDE ^a	61–85	683–799	[25,62–65]
Ti–Nb–Zr	L-PBF	65–85	916–1155	[26,27,66]
Ti–Nb–Ta–Zr (TNTZ)	L-PBF	64	680	[28,67]
Ti–Nb–Zr–Sn (Ti2448)	L-PBF/E-PBF ^{**}	53	665–950	[29,30,68]
Ti–Ta (10–50 wt %)	L-PBF	65–115	509–1186	[35,37,41,69,70]

^a L-DDE = laser directed energy deposition ^{**} E-PBF = electron beam powder bed fusion.

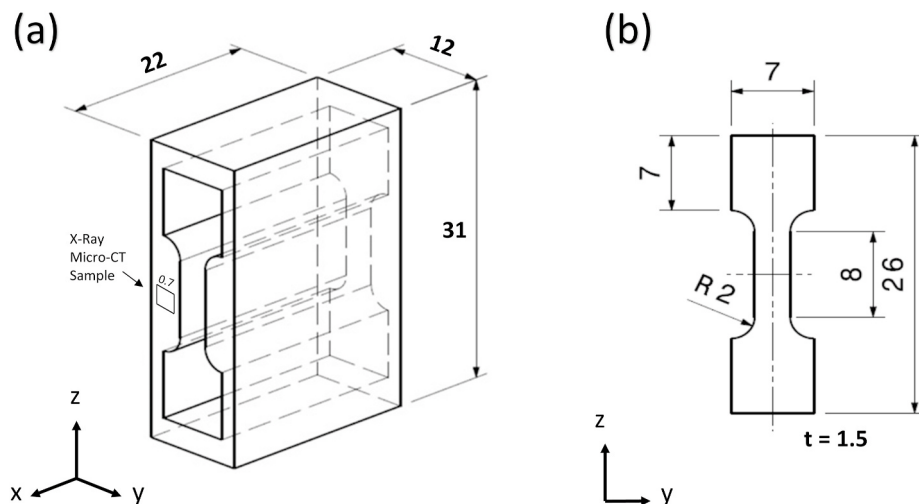


Fig. 1. Geometries of the printed block (a) and the machined fatigue samples (b). Measurements are given in mm. Positioning of the samples used for X-ray Micro-CT analysis is shown in (a) (not to scale). X-ray Micro-CT samples were 0.7 × 0.7 × 4 mm³.

step ion beam polishing at 300 μA and 7 kV for 10 min and then 100 μA and 3 kV for 15 min. Inverse pole figure (IPF) maps were created using a JEOL 7001F FEG scanning electron microscope (SEM). The fractography analysis was conducted using a Zeiss ULTRA GEMINI high-resolution SEM with back scattered electron and electron dispersive X-ray (EDX) detectors to investigate Ta distributions.

2.2. X-ray Micro-CT

X-ray Micro-CT was performed on the 0.7 mm × 0.7 mm × 4 mm samples cut with a diamond wire saw from the residual fatigue block material. Samples were ground with P1000 grit paper before Micro-CT analysis with a Zeiss Xradia Versa 520. The data obtained was reconstructed and analysed using Avizo 9.4 software. Measurements were taken with an acceleration voltage of 140 kV, power of 10 W and a voxel size of 2.20 μm. Afterwards the sample geometries were segmented using a grey-thresholding tool. Tantalum particles and pores were differentiated by grey values and contrasted with the titanium. Subsequently, data was cleaned to remove minor artefacts. Due to voxel size and cleaning, pore or tantalum particles with a size less than 5 μm are not reliable and therefore excluded from the data. The equivalent diameter was calculated describing the same volume fraction of each feature in a round shape. Avizo 9.4 software was used to calculate the average sphericity of the particles and pores, using the measured volume and surface area of the features. The reader is directed to Avizo 9.4 software documentation for the relevant equations.

2.3. Fatigue testing

Low-cycle fatigue tests were conducted using a digitally controlled servo-hydraulic load frame, with a load ratio of $R = -1$, under strain-controlled conditions. Total strain amplitudes of $\Delta\varepsilon/2 = \pm 0.5\%$, $\pm 0.65\%$ and $\pm 0.8\%$ were considered, with a constant strain rate of $6 \times 10^{-3} \text{ s}^{-1}$. An MTS miniature extensometer with a gauge length of 5 mm was attached to the surface of each sample. Two samples were tested for each condition, due to the high cost of source materials. The lack of scatter in data and consistent fatigue life trends between strain levels supported reproducibility. One representative curve for each condition is shown in Fig. 4.

3. Results

3.1. Microstructure

The microstructure of AM materials is known to severely affect the fatigue behaviour. For instance, in the case of Ti–6Al–4V fatigue crack initiation was observed in the α phase and, hence, generally finer α microstructures resulted in superior fatigue performance [71]. In the present study, the microstructure of the single melt and remelt samples is studied in the y-z plane, see Fig. 2. Both samples display an α' lath microstructure with no statistical difference in lath size. An average lath length of $5.7 \pm 2.7 \mu\text{m}$ and a width of $0.6 \pm 0.3 \mu\text{m}$ were determined by measuring a selection of one hundred laths from different regions, using ImageJ software. The remelt scan causes a subtle randomisation of lath orientation as noted in previous work [35], however, here to a lesser degree than in previous studies.

3.2. Micro-CT

The fatigue behaviour of AM material is known to depend on process induced porosity. Micro-CT analysis was performed to assess the porosity and partially melted Ta percentage of the single and remelt scan conditions. Fig. 3 shows the Micro-CT image analysis and resulting size distributions of (a) the porosity and (b) the Ta particles. When the material is fabricated with the single scan strategy a porosity level of $0.15 \pm 0.01 \text{ vol } \%$ is determined. Fig. 3a shows that the pores are evenly distributed throughout the material and the measured average pore diameter is around 15 μm. Only a few larger pores with sizes between 30 and 40 μm could be detected. The average sphericity of the particles was 0.96 ± 0.10 , showing the majority are very close to spherical and hence likely related to gas entrapment. The remelt strategy visibly influenced the overall porosity level and led to an increase to $0.37 \pm 0.01 \text{ vol } \%$. While the remelting led to an increase in the number of smaller pores, the average pore diameter remained 15 μm, see Fig. 3a. Larger pores, which are most detrimental to the fatigue performance of the material, remained almost unchanged.

Secondly, Micro-CT was used to analyse the volume fraction of the partially melted Ta particles. Our previous study [35] showed that the remelt strategy reduced the Ta particles to 0.25%. This result was obtained using optical microscopy analysis of the cross-sections of the sample. Here, Micro-CT analysis is applied to study the volume fraction of the Ta particles and simultaneously depict their distribution within the sample. It can be seen in Fig. 3b that the single scan strategy results in samples with $2.07 \pm 0.01 \text{ vol } \%$ of homogeneously distributed Ta

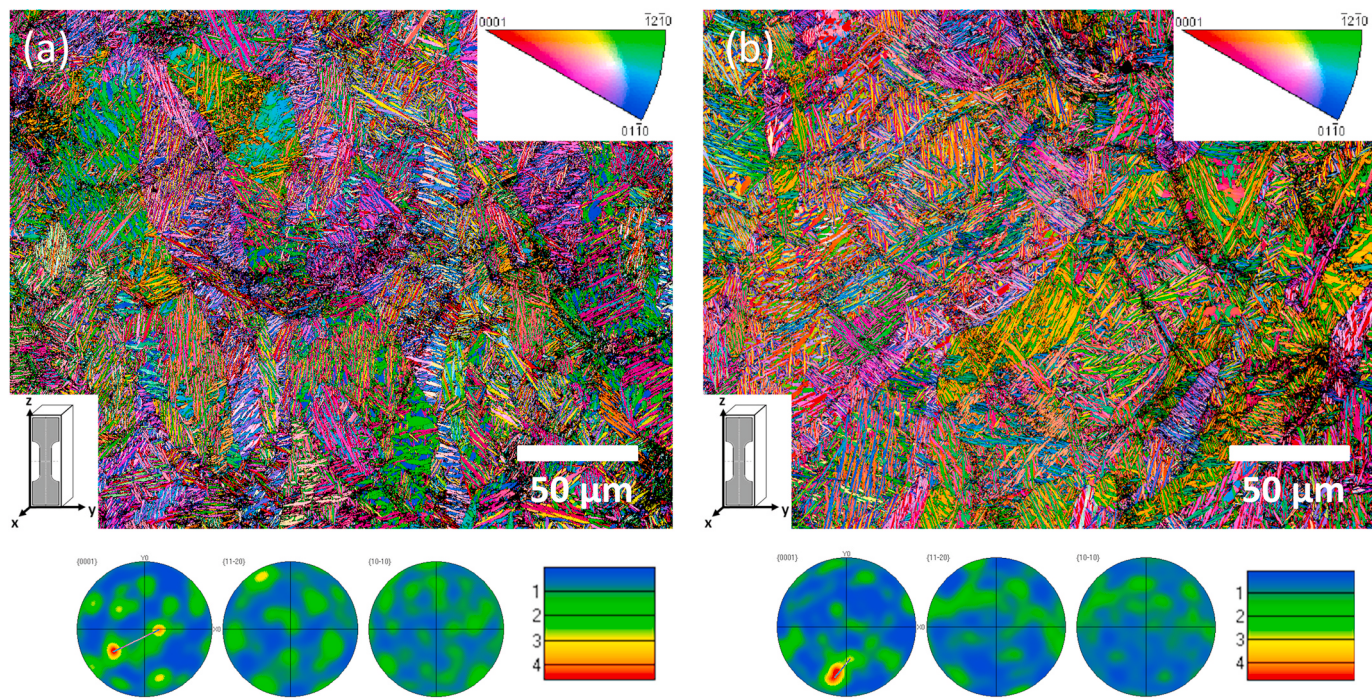


Fig. 2. Inverse pole figure (IPF) maps and corresponding pole figure plots of y-z plane α' martensite laths in (a) single melt and (b) remelt conditions.

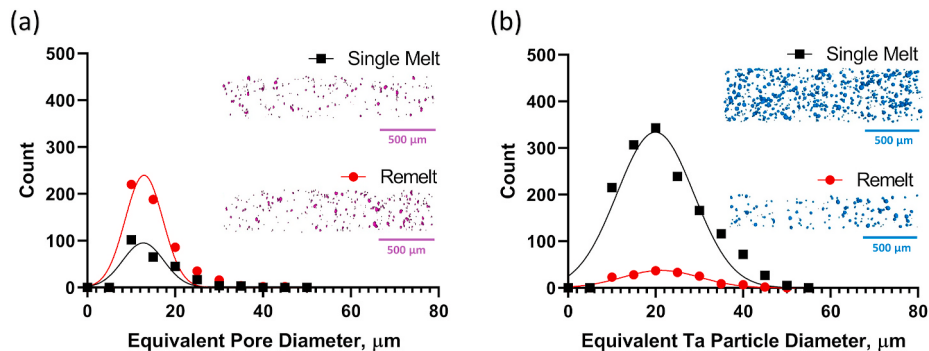


Fig. 3. Micro-CT analysis of (a) porosity and (b) distribution of partially melted Ta particles for the single melt and remelt conditions. The remelt causes a large reduction in Ta particles and only a minor increase in porosity.

particles. The remaining Ta particles are spherical in shape and correspond well with the particle size and distribution of the original powder. The fraction of Ta particles over 45 μm in the original powder was 0.7% [35]. In the single scan sample 0.3% of the remaining particles were over 45 μm and none remained over 45 μm in the remelt sample. The remelt scan significantly reduced the volume fraction of remaining Ta particles down to 0.22 vol %, while the particle size and distribution remained unchanged.

Table 3 summarises the results of the Micro-CT analysis of the sample porosity and volume fraction of partially melted Ta particles. Reasons for changes in the porosity and reduction of the volume fraction of the Ta particles will be presented in section 4.2.

3.3. Low-cycle fatigue

Implant materials often experience fully reversed stress-strain cycles during their use, imposed by the complex stresses applied by body geometries. Hence, the cyclic stress response of the L-PBF Ti25Ta alloy was characterised, both in single melt and remelt conditions, and is displayed in Fig. 4. The alloy was tested at a low, medium and high strain level, covering elastic to plastic regions of behaviour in the LCF regime.

In order to avoid buckling of the thin samples the load was increased stepwise until the prescribed strain amplitude was reached after approximately 10–25 cycles.

The initial cycles are characterised by a steady increase of the stress amplitude, due to the stepwise increase in load. This initial behaviour is followed by a stable stress plateau for both the single melt and remelt conditions at the lowest strain amplitude of $\Delta\epsilon/2 = \pm 0.5\%$ and for the single melt condition at the medium strain amplitude of $\Delta\epsilon/2 \pm 0.65\%$, suggesting fully elastic behaviour. In contrast, cyclic softening can be observed upon both scan strategy conditions at the highest strain amplitude of $\Delta\epsilon/2 = \pm 0.8\%$ and very slightly for the remelt scan sample at medium strain amplitude of $\Delta\epsilon/2 \pm 0.65\%$. The softening behaviour indicates that the cyclic loading includes minor plasticity, implying that the cyclic yield strengths of the single melt and remelt materials are less than 540 MPa and 690 MPa, respectively. This is in line with earlier studies, which found the monotonic yield strength of the single melt and remelt materials to be 426 ± 14 MPa and 545 ± 9 MPa, respectively [35]. The remelt samples showed a higher stress amplitude than the single melt samples at each strain level, ultimately pointing to a combination of higher strength and elastic modulus.

The half-life hysteresis loops, Fig. 4b–c, confirmed plastic

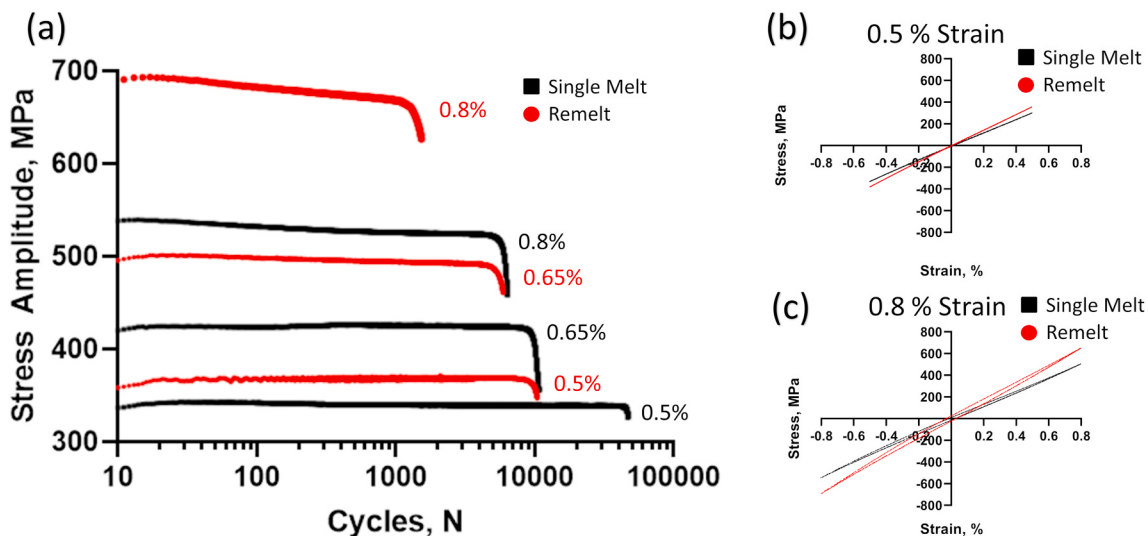


Fig. 4. (a) Cyclic deformation of single and remelt scan Ti25Ta for strain amplitudes of $\Delta\epsilon/2 = \pm 0.5\%$, $\pm 0.65\%$ and $\pm 0.8\%$. Half-life hysteresis loops (b) at $\pm 0.5\%$ strain amplitude and (c) at $\pm 0.8\%$ strain amplitude show an increase in elastic modulus in the remelt samples.

Table 3
Fraction of Ta particles and porosity detected using Micro-CT analysis.

	Partially Melted Ta Volume (%)	Porosity Volume (%)
Ti25Ta Single melt	2.07 ± 0.01	0.15 ± 0.01
Ti25Ta Remelt	0.22 ± 0.01	0.37 ± 0.01

deformation at the 0.8% strain amplitude by obvious loop opening. The gradient of the half-life hysteresis loops was used to calculate the elastic modulus revealing 65.4 ± 1.9 GPa and 76.8 ± 3.3 GPa, for the single melt and remelt samples, respectively. The remelt has caused an increase in elastic modulus, most likely due to increased solutionised tantalum.

Finally, the remelt samples consistently show a lower number of cycles to failure, compared with the single melt samples, at each strain level. The reduced fatigue life and higher elastic modulus of the remelt samples suggest that the remelt scanning strategy is less suited for implant manufacture compared with the single melt strategy.

3.4. Fractography

Fatigue failure in AM parts is known to depend strongly on the presence of processing induced defects. As noted in section 3.2, the L-PBF Ti25Ta material includes the remnants of Ta particles within the matrix. The effect of these particles on fatigue crack initiation was investigated through secondary electron (SE) and EDX analysis of the fatigue fracture surfaces.

The fracture surfaces of the single and remelt samples fatigued at low strain amplitude, Fig. 5a and b respectively, are clearly characterised by stable fatigue crack growth zones (upper right part of both fracture surfaces). The higher defect concentration in the remelt sample is validated through a larger number of pores visible on the fracture surface. The pores appear as spherical, ribbed indentations, about $20 \mu\text{m}$ in diameter, in line with the Micro-CT analysis. The striations within the fatigue crack propagation zone of each of the single melt and remelt samples indicate that the fatigue crack was initiated by a process induced defect in direct vicinity of the sample surface. At higher strain amplitudes, Fig. 5c and d, a smaller fatigue crack propagation zone is seen, and multiple crack initiation sites can be observed on each surface (highlighted by rectangles).

Higher magnification SEM and EDX analysis of the fracture surfaces was used to investigate whether defects spatially correspond to

remaining Ta particles, particularly as some of the highlighted defects contained what appeared to be particles inside the pore, Fig. 5a and d (insets). The EDX analysis, Fig. 6, showed no relationship between pores and Ta particle positioning in either the single melt or remelt conditions, hence, only the remelt condition is shown. This suggests that the Ta particles did not contribute to the formation of process induced defects. In addition, the Ta particles, even in highly deformed zones, show no decohesion from the matrix and, hence, are unlikely to act as crack initiation sites. The particles observed inside voids, were also assessed for their chemical nature and were found to consist of nominal matrix composition.

4. Discussion

4.1. Effects of the remelt microstructure

One important aspect of this study is to correlate the effect of the remelt strategy on the fatigue performance given that the remelt strategy has shown to disrupt lath orientation. The randomisation of lath orientation may contribute to the reduced fatigue performance of the remelt sample, due to lower ductility. Reduced ductility was noted in monotonic testing of the remelt samples in previous work [35] however the mechanism was not elucidated. Deformation occurs via $<\mathbf{a}>$ slip and $\{1\ 0\ \bar{1}\ 1\}$ twinning in α' titanium [72], however, twinning can be retarded by stacking faults, and small amounts of other phases, such as β , at the interfaces of the twin [73]. Crack nucleation and propagation are affected by the distribution of stress throughout the microstructure and, hence, here it is hypothesised that the increased interface mismatches caused by lath randomisation promote dislocation pileup and brittle failure in the remelt condition. Hence, crack propagation is enhanced during fatigue cycling and the remelt sample shows a decreased fatigue life.

4.2. Increase in elastic modulus in remelt samples

The remelt scan showed an average 18% increase in stress response over the three strain amplitudes and an average 17% increase in elastic modulus, as calculated from the hysteresis loops. The remelt scan facilitates further Ta diffusion leading to increased solution strengthening and crystallographic changes. In the Ti-Ta system, as the fraction of Ta increases from 0 to 25%, Zhou et al. [61] showed that the elastic modulus decreases. This was attributed to the existence of the α' phase,

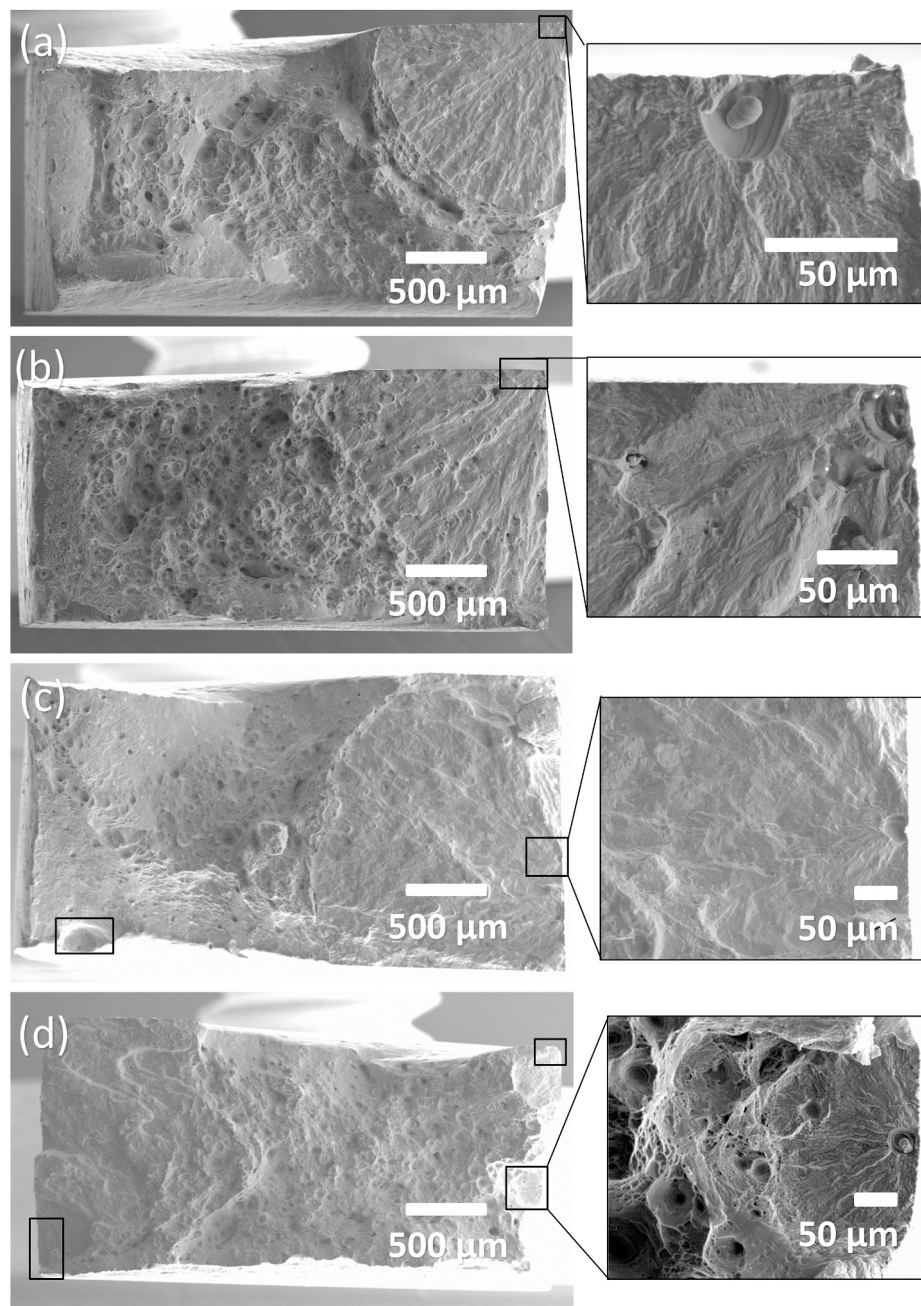


Fig. 5. Fractography of (a) (c) single melt and (b) (d) remelt Ti25Ta surfaces after LCF at low strain ($\Delta\epsilon/2 = \pm 0.5\%$) (a) (b) and high strain ($\Delta\epsilon/2 = \pm 0.8\%$) (c) (d). Cracks are shown to initiate from surface defects.

which increases in unit cell volume as more tantalum is added to the structure, ultimately decreasing the elastic modulus. However, at 30 wt % Ta the elastic modulus once again increases. For such alloys, presence of the α'' phase, as well as further phases such as ω phase, have been revealed [74]. Here, it is likely that the remelt scan is facilitating the formation of small volume fractions of α'' phase on the local scale.

The α'' phase is generally only seen in compositions between 25 and 60 wt % Ta [40,75,76]. However, as there are still partially melted Ta particles in both the single melt and remelt samples, there are likely diffusion zones in both samples which meet this composition requirement. Upon remelting, the diffusion zones become larger and the volume fraction of the sample falling into this composition range will grow, increasing the elastic modulus of the bulk sample. The presence of α'' in the remelt Ti25Ta material was shown in Ref. [35] through TEM analysis, however no increase in elastic modulus was measured through

ultrasonic testing. This discrepancy may be attributed to the method of testing used. Whilst ultrasonic modulus testing is generally perceived as the more accurate method of modulus measurement [22], the method may have been effected by the inhomogeneity of the material with partially melted Ta particles leading to wave scattering. Here, the modulus calculated from the half-life hysteresis loops is deemed more representative of the bulk material.

The increase in strength and elastic modulus of the remelt sample results in a higher stress response at the same strain levels, as compared with the single melt sample. Whilst the increase in elastic modulus is not ideal for biomedical applications, the observed value of 76.8 ± 3.3 GPa is still well within the range of many β -type titanium alloys and much below that of Ti-6Al-4V [22].

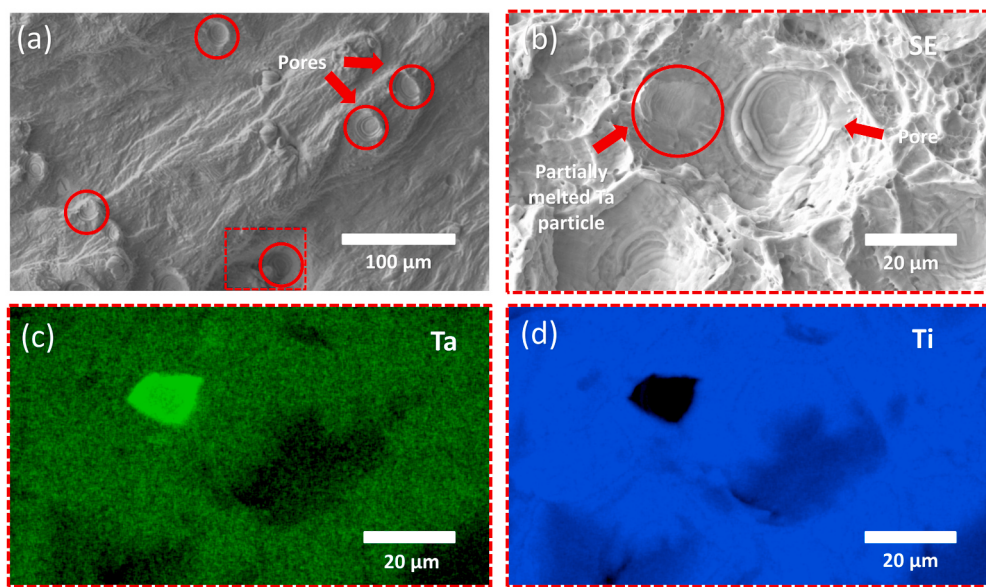


Fig. 6. SE micrographs at low (a) and high (b) magnification showing process induced defects. EDX element maps showing Ta (c) and Ti (d) in the area highlighted in the SE image in (b).

4.3. Increase in porosity for remelt samples

The remelt scan caused an increase in homogeneity, as indicated by the reduction of the remaining number of Ta particles in the alloy. However, this was coupled with a minor increase in porosity from $0.15 \pm 0.01\%$ to $0.37 \pm 0.01\%$. This increase still results in a density of 99.63%, a level representative of well processed ‘as-built’ L-PBF titanium alloys [77–80].

The initial parameter study for mixed powder Ti25Ta showed no increase in porosity when the remelt scan was applied, for identical printing parameters [35]. However, it must be noted that the initial parameter study used optical microscopy to measure the porosity, which is less reliable than Micro-CT observations. Generally, literature studies show that a remelt scan increases part density when identical scanning parameters are used for the single scan and the remelt scan [45,47,48, 52,54,57,81,82]. For these studies, it is likely that the single melt scanning conditions bordered on a lower energy density. As a result, a single scan may result in porosity due to insufficient melting, and the remelt scan induces liquid flow a second time to fill in previous defects.

When scanning parameters differ between the single and remelt scans, it is shown that the part density can decrease, particularly if the energy density of the remelt scan is raised [45,55,82]. Higher energy density of the remelt scan can lead to vaporisation, despite the reduced laser absorption. It is hypothesised that the temperature of the melt pool rises as heat cannot be conducted quickly enough away from the melting zone facilitating material vaporisation. This effect may be seen primarily in titanium alloys due to the low thermal conductivity of titanium ($21.9 \text{ W} (\text{m K})^{-1}$) compared with other commonly AM metals such as aluminium alloys ($237 \text{ W} (\text{m K})^{-1}$) and steels ($80.2 \text{ W} (\text{m K})^{-1}$) [83].

The present work is the only study to show an increase in porosity using the same scanning parameters for the remelt scan. However, the presence of porosity also in the single scan state may suggest that vaporisation may have already occurred during the single melt scan. Therefore, a second application of the laser with the same parameters would likely compound the porosity. The optimal parameters chosen in Ref. [35] were on the cusp of the transition to keyhole formation and a slight variation to the powder composition or to the laser power, may have caused a shift in energy density.

4.4. Changes in fatigue performance of remelt samples

The present work aims to improve the mechanical properties of the L-PBF Ti25Ta mixed powder alloy by introducing a remelt scanning strategy to enhance alloy homogeneity *in situ*. The remelt scan is successful at reducing the volume fraction of remaining Ta particles, as shown in Fig. 3 and increases alloy strength by 28%. However, Fig. 4 shows that the remelt scan results in a decrease in the number of cycles to failure for a given strain amplitude. This is likely due to a combination of several factors including; ductility, porosity, residual stress and dislocation density.

Whilst comparing the factors which contribute to fatigue failure, it must be considered that the strain amplitudes used in this study fall mainly into the LCF regime. The LCF performance tends to be dominated by crack propagation life, whilst (very) high-cycle fatigue performance tends to be dominated by crack initiation life [12,84]. Whilst microstructural features can affect fatigue performance to different degrees in either regime, the failure of the samples in the present study is likely attributed to crack propagation, which is highly dependent on material ductility.

It was shown in previous studies [35] that under quasi-static tensile loading the remelt samples exhibited a 28% increase in material yield strength, however, a 56% reduction in elongation to fracture. A decrease in ductility leads to an increase in notch sensitivity [3], as well as faster crack propagation [2], due to a reduced zone of plastic deformation in front of the crack tip. The reduced ductility is hence a severe contributing factor to the inferior performance of the remelt samples at all strain amplitudes. In addition, the remelt samples are characterised by an increase in alloy strength and elastic modulus. As testing was conducted under strain control, the resulting stress amplitude was higher for the remelt scan fatigue samples than for the single melt samples. Samples tested to higher forces are expected to fail at a lower number of cycles.

Although the samples were tested in the LCF regime, the effect of porosity and partially melted Ta particles acting as crack initiation sites must still be considered. The remelt scan reduces the number of remaining Ta particles, however, at the same slightly increases the pore concentration, as shown in Fig. 3. Reducing the number of remaining Ta particles could increase fatigue performance, however, any improvement is possibly concealed by the detrimental effect of the increased porosity. The fractography analysis, Fig. 5, shows that in all samples the

fatigue cracks initiate at pores and none at remaining Ta particles. Hence, the reduced amount of Ta particles in the remelt sample has a negligible effect on the fatigue life.

Additionally, the number count increase in pores caused by the remelt scan (317 pores) is less than the decreased number count of Ta particles (1326 Ta particles). The overall number of crack initiation sites is hence decreased by the remelt scan. However, when comparing the shape and size of these features, the Ta particles show an average particle diameter of 22 μm , larger than that of the pores, 15 μm . Larger defects tend to be most detrimental to fatigue life [85,86], however the cohesion between the Ta particles and the matrix result in them being less critical defects. The porosity increase caused by the remelt scan had little effect on the fatigue life, likely due to the porosity size distribution. Romano et al. [85,86] have shown that surface defects above 120 μm in diameter significantly alter the relationship between pore size and fatigue life. The maximum pore diameter in the single melt sample was 32 μm , whilst that of the remelt sample was 40 μm . This minor increase in the maximum pore size was shown to have negligible effect on the fatigue performance and agrees well with the studies conducted by Romano et al. [85,86]. Furthermore, the remelt scan caused a slight increase in pore sphericity 0.96–0.97 which may have decreased the stress concentration capacity of these defects. Overall, it is unlikely the increase in porosity has a large impact on the reduced fatigue life of the remelt samples.

Residual stress states for each scanning condition should also be considered. Residual stresses are inherent in L-PBF processing as the high temperature gradient between the substrate and melt pool leads to high solidification rates. Literature studies show that remelting can be employed to reduce residual stress, however the efficiency depends on the scanning parameters. Studies using identical scanning parameters for the remelt scan, as done in the present study, show an initial increase in residual stress in the range of 22–68% upon remelting [45,54,82]. However, all samples tested in the present work were cut by EDM from a printed block, likely relieving L-PBF process induced residual stresses [87–89]. Further analysis is needed to determine the residual stress state in the EDM samples however this is beyond the scope of the present study. Here, it is assumed that residual stresses have a minor impact on the fatigue lives determined.

Finally, a difference in dislocation density may contribute to the earlier failure of the remelt samples, due to enhanced cyclic softening. Cyclic softening was observed in both the single melt and remelt samples at 0.8% strain amplitude. However, very slight cyclic softening (of 498–491 MPa) could be seen in the remelt sample at 0.65% strain amplitude, whilst none was observed at the same strain amplitude for the single melt sample. At 0.65% strain amplitude the single melt sample stress response (423 MPa) was much closer to its yield strength (426 ± 15 MPa) [35] than the remelt scan sample (498 MPa and 545 ± 9 MPa [35], respectively). This seems to be contradictory at first glance, however, could indicate a difference in dislocation density. If the remelt samples are characterised by a higher dislocation density, dislocation annihilation may be enhanced during cyclic loading, resulting in pronounced softening. Peak broadening in XRD analysis was used to attempt the quantification of residual stress and dislocation density, however, no difference in peak broadening could be quantified between the single and remelt conditions.

In conclusion, the remelt scan does not lead to improvement of the fatigue life of L-PBF processed mixed powder Ti25Ta. The reduction of volume fraction of remaining Ta particles, promoted by the remelt scan, had a negligible effect on the fatigue performance. The reduced ductility of the remelt sample dominated failure in the LCF regime due to enhanced crack propagation.

4.5. Fatigue performance of Ti25Ta compared with other alloys

The L-PBF Ti25Ta material performs well in fatigue when compared with other common L-PBF produced biomedical alloys, Fig. 7. For this

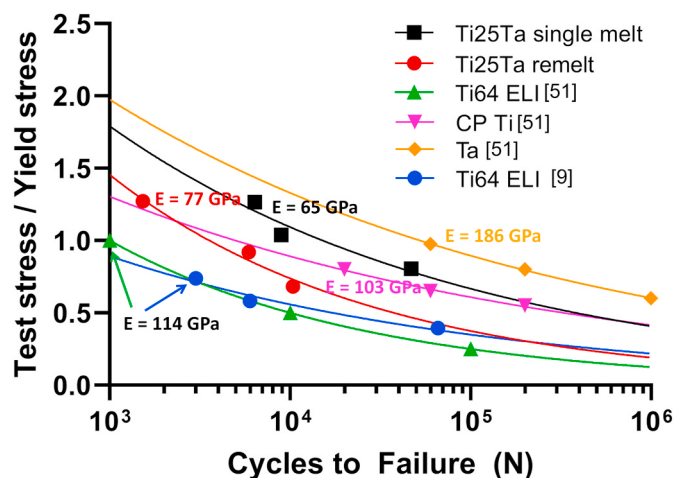


Fig. 7. Comparison of Wohler-type curves of Ti25Ta L-PBF material to L-PBF Ti-6Al-4V ELI, CP Ti and Ta. Stress amplitudes were normalised by yield stress. Surface conditions of the materials differ. See text for details.

comparison, the fatigue strength is normalised by the yield strength of each material, allowing for comparison with porous structures [32,38,90]. The data used to create Fig. 7 is included in the supplementary data.

The fatigue samples in this study were machined from a block. It is well documented that the surface roughness of ‘as-built’ material reduces the fatigue life of AM samples significantly [8,13–15]. The materials used for comparison from literature [32,38,90] were tested with an ‘as-built’ surface finish and, hence, very likely are suffering roughness induced minor performance. This data is nonetheless necessary for comparison as the data available for L-PBF produced Ta and grade 1 CP Ti is limited. The Ti-6Al-4V ELI data from Ref. [90] is included and compared with the Ti-6Al-4V ELI data from Refs. [6], where the material had a fine surface finish ($R_a = 6.8 \mu\text{m}$). Machined surfaces generally fall in the range of $R_a = 2–10 \mu\text{m}$ [91–94], however, it can be directly deduced from the fractography, Fig. 5, that defects up to 25 μm are present in the direct vicinity of the surface of the machined samples from the present study. Furthermore, the material from Ref. [6] was heat treated to relieve residual stress, whilst the material in the present work was not. Thermal post treatments were not investigated in the present work, as the aim of the study was to explore scanning strategies which could increase alloy homogeneity during building avoiding additional post treatments.

The Ti25Ta single melt material shows the second highest normalised stress for any given number of cycles to failure (Fig. 7). The Ti25Ta single melt is only outperformed by pure Ta and shows superior properties to CP Ti. This can be attributed to the solid solution strengthening of the α' Ti by Ta atoms, without largely reducing ductility. However, the pure Ta and CP Ti both display almost twice the elastic modulus of the Ti25Ta alloy. This large reduction in elastic modulus, without sacrificing fatigue performance, reveals the Ti25Ta single melt material as a very promising material for implant applications. The remelt scan material also performs well, however, is outperformed by the single melt material in this examination, due to the factors discussed in section 4.3.

The Ti-6Al-4V ELI data shows only a small difference between the fatigue life of the ‘as-built’ (triangle marker) and the fine surface finish (circle marker) conditions. As expected, the material with the superior surface finish shows a higher stress response at a higher number of cycles to failure, as failure in the high-cycle fatigue regime is dominated by crack initiation. Compared with the Ti25Ta material, the Ti-6Al-4V shows a lower normalised stress response, due to its much higher static strength ($\sigma_y = 863$ MPa) [38]. As the Ti25Ta material shows an improved normalised fatigue response, as well as a much lower elastic modulus, it would be well suited for implants subjected to lower stresses, such as cranio/maxillofacial, whereas Ti-6Al-4V may still be required

for high stress applications.

LCF testing reveals how the investigated materials perform under high stresses and, thus, provides an indication as to when processes such as cyclic softening may occur. The geometry and features of implants can vary widely, as well as the stress state. New implants are investigating scaffold structures to further reduce elastic modulus and to promote tissue regrowth [95–97]. Scaffolds can possess very small strut sizes and, hence, it is important to understand the material behaviour under high stresses. The data acquired in the present work is a critical input for finite element analysis (FEA) to help simulate and design implants under realistic loading conditions. It is still necessary for the material to be tested in the high-cycle regime. Particularly for implants such as mandible implants, the number of cycles experienced will be well above 10^6 cycles.

5. Conclusions

Ti25Ta fatigue samples were successfully additively manufactured by L-PBF utilising single melt and remelt scan strategies. This work demonstrates that the L-PBF Ti25Ta displays promising fatigue properties for biomedical implant applications. The specific conclusions drawn are:

- The yield stress normalised fatigue performance of the Ti25Ta material is superior to pure Ti and Ti-6Al-4V, due to solution strengthening of the titanium and retained ductility. At a normalised stress of 1.0, the Ti25Ta single melt material showed a significant increase in the number of cycles to failure of 2×10^4 , compared to 4×10^3 for CP Ti and 1×10^3 for Ti-6Al-4V. Furthermore, the Ti25Ta alloy shows almost half the elastic modulus (65.4 ± 1.9 GPa) of the commonly used alloys (~110 GPa).
- The L-PBF Ti25Ta microstructure displayed an α' lath microstructure with average lath length of 5.7 ± 2.7 μm and width of 0.6 ± 0.3 μm , for both scanning strategies. However, the remelt scan strategy affected the degree of randomisation of the orientation of the laths, causing lower ductility.
- The remelt scan increased the yield strength by 28% and the elastic modulus by 17% due to enhanced solutionised Ta. It also decreased partially melted Ta particles, increasing the homogeneity of the alloy, which had a negligible effect on the fatigue life.
- The reduction in fatigue performance between the remelt scan and the single melt scan which was approximately 5×10^3 cycles at high stress to 8×10^4 cycles at low stress levels, was attributed to reduced ductility, as well as increased residual stresses and dislocation densities.
- Process induced defects were identified as the dominant fatigue crack initiation sites.

CRediT authorship contribution statement

Erin G. Brodie: Conceptualization, Methodology, Formal analysis, Investigation, Writing - original draft, Writing - review & editing. **Julia Richter:** Investigation, Formal analysis, Writing - original draft, Writing - review & editing. **Thomas Wegener:** Investigation, Formal analysis, Writing - original draft, Writing - review & editing. **Thomas Niendorf:** Conceptualization, Writing - review & editing, Funding acquisition. **Andrey Molotnikov:** Conceptualization, Writing - review & editing, Supervision, Funding acquisition.

Declaration of competing interest

The authors declare that they have no known competing financial interests or personal relationships that could have appeared to influence the work reported in this paper.

Acknowledgments

EGB would like to acknowledge the Monash Centre for Electron Microscopy. This project is funded by the ARC Research Hub for Transforming Australia's Manufacturing Industry through High Value Additive Manufacturing (IH130100008). AM would also like to acknowledge the support of the Garnett Passe and Rodney Williams Memorial Foundation 2019 Conjoint Grant (2019CG_Sigston_Molotnikov). TN acknowledges financial support by AiF/IGF (Contract # 19689 BG/2).

Appendix A. Supplementary data

Supplementary data to this article can be found online at <https://doi.org/10.1016/j.msea.2020.140228>.

Data availability

The raw/processed data required to reproduce these findings cannot be shared at this time as the data also forms part of an ongoing study.

References

- [1] H. Attar, S. Ehtemam-Haghghi, N. Soro, D. Kent, M.S. Dargusch, Additive manufacturing of low-cost porous titanium-based composites for biomedical applications: advantages, challenges and opinion for future development, *J. Alloys Compd.* 827 (2020) 154263.
- [2] S. Leuders, M. Thöne, A. Riemer, T. Niendorf, T. Tröster, H.A. Richard, H.J. Maier, On the mechanical behaviour of titanium alloy TiAl6V4 manufactured by selective laser melting: fatigue resistance and crack growth performance, *Int. J. Fatig.* 48 (Supplement C) (2013) 300–307.
- [3] P. Edwards, M. Ramulu, Fatigue performance evaluation of selective laser melted Ti-6Al-4V, *Mater. Sci. Eng., A* 598 (Supplement C) (2014) 327–337.
- [4] L. Parry, I.A. Ashcroft, R.D. Wildman, Understanding the effect of laser scan strategy on residual stress in selective laser melting through thermo-mechanical simulation, *Addit. Manuf.* 12 (2016) 1–15.
- [5] S. Beretta, S. Romano, A comparison of fatigue strength sensitivity to defects for materials manufactured by AM or traditional processes, *Int. J. Fatig.* 94 (2017) 178–191.
- [6] M. Benedetti, V. Fontanari, M. Bandini, F. Zanini, S. Carmignato, Low- and high-cycle fatigue resistance of Ti-6Al-4V ELI additively manufactured via selective laser melting: mean stress and defect sensitivity, *Int. J. Fatig.* 107 (2018) 96–109.
- [7] D. Greitemeier, F. Palm, F. Syassen, T. Melz, Fatigue performance of additive manufactured TiAl6V4 using electron and laser beam melting, *Int. J. Fatig.* 94 (2017) 211–217.
- [8] C.N. Kelly, N.T. Evans, C.W. Irvin, S.C. Chapman, K. Gall, D.L. Safranski, The effect of surface topography and porosity on the tensile fatigue of 3D printed Ti-6Al-4V fabricated by selective laser melting, *Mater. Sci. Eng. C* 98 (2019) 726–736.
- [9] J.H. Zuo, Z.G. Wang, E.H. Han, Effect of microstructure on ultra-high cycle fatigue behavior of Ti-6Al-4V, *Mater. Sci. Eng., A* 473 (1) (2008) 147–152.
- [10] Y. Furuya, E. Takeuchi, Gigacycle fatigue properties of Ti-6Al-4V alloy under tensile mean stress, *Mater. Sci. Eng., A* 598 (2014) 135–140.
- [11] H. Yokoyama, O. Umezawa, K. Nagai, T. Suzuki, Distribution of internal crack initiation sites in high-cycle fatigue for titanium alloys, *ISIJ Int.* 37 (12) (1997) 1237–1244.
- [12] J. Günther, D. Krewerth, T. Lippmann, S. Leuders, T. Tröster, A. Weidner, H. Biermann, T. Niendorf, Fatigue life of additively manufactured Ti-6Al-4V in the very high cycle fatigue regime, *Int. J. Fatig.* 94 (Part 2) (2017) 236–245.
- [13] Z. Chen, S. Cao, X. Wu, C.H.J. Davies, 13 - surface roughness and fatigue properties of selective laser melted Ti-6Al-4V alloy, in: F. Froes, R. Boyer (Eds.), *Additive Manufacturing for the Aerospace Industry*, Elsevier, 2019, pp. 283–299.
- [14] H. Yu, F. Li, Z. Wang, X. Zeng, Fatigue performances of selective laser melted Ti-6Al-4V alloy: influence of surface finishing, hot isostatic pressing and heat treatments, *Int. J. Fatig.* 120 (2019) 175–183.
- [15] J. Zhang, A. Fatemi, Surface roughness effect on multiaxial fatigue behavior of additive manufactured metals and its modeling, *Theor. Appl. Fract. Mech.* 103 (2019), 102260.
- [16] B.D. Boyan, R. Batzer, K. Kieswetter, Y. Liu, D.L. Cochran, S. Szmuckler-Moncler, D.D. Dean, Z. Schwartz, Titanium surface roughness alters responsiveness of MG63 osteoblast-like cells to 1 α ,25-(OH) $_2$ D $_3$, *J. Biomed. Mater. Res.* 39 (1) (1998) 77–85.
- [17] D.J. Cohen, A. Cheng, K. Sahingur, R.M. Clohessy, L.B. Hopkins, B.D. Boyan, Z. Schwartz, Performance of laser sintered Ti-6Al-4V implants with bone-inspired porosity and micro/nanoscale surface roughness in the rabbit femur, *Biomed. Mater.* 12 (2) (2017), 025021.
- [18] L. Shan, H.K. Abdul Amir, M.S.H. Al-Furjan, W. Weng, Y. Gong, K. Cheng, M. Zhou, L. Dong, G. Chen, M.S. Takriff, S. Abu Bakar, In situ controlled surface microstructure of 3D printed Ti alloy to promote its osteointegration, *Materials* 12 (5) (2019).

- [19] X. Feng, G. Lin, C.X. Fang, W.W. Lu, B. Chen, F.K.L. Leung, Bone resorption triggered by high radial stress: the mechanism of screw loosening in plate fixation of long bone fractures, *J. Orthop. Res.* 37 (7) (2019) 1498–1507.
- [20] L. Kunčická, R. Kocich, T.C. Lowe, Advances in metals and alloys for joint replacement, *Prog. Mater. Sci.* 88 (2017) 232–280.
- [21] M. Tane, S. Akita, T. Nakano, K. Hagihara, Y. Umakoshi, M. Niinomi, H. Nakajima, Peculiar elastic behavior of Ti-Nb-Ta-Zr single crystals, *Acta Mater.* 56 (12) (2008) 2856–2863.
- [22] M. Niinomi, M. Nakai, J. Hieda, Development of new metallic alloys for biomedical applications, *Acta Biomater.* 8 (11) (2012) 3888–3903.
- [23] M. Niinomi, Design and development of metallic biomaterials with biological and mechanical biocompatibility, *J. Biomed. Mater. Res.* 107 (5) (2019) 944–954.
- [24] H. Liu, M. Niinomi, M. Nakai, S. Obara, H. Fujii, Improved fatigue properties with maintaining low Young's modulus achieved in biomedical beta-type titanium alloy by oxygen addition, *Mater. Sci. Eng., A* 704 (2017) 10–17.
- [25] J.C. Wang, Y.J. Liu, P. Qin, S.X. Liang, T.B. Sercombe, L.C. Zhang, Selective laser melting of Ti-35Nb composite from elemental powder mixture: microstructure, mechanical behavior and corrosion behavior, *Mater. Sci. Eng., A* 760 (2019) 214–224.
- [26] L. Zhou, T. Yuan, R. Li, J. Tang, M. Wang, L. Li, C. Chen, Microstructure and mechanical performance tailoring of Ti-13Nb-13Zr alloy fabricated by selective laser melting after post heat treatment, *J. Alloys Compd.* 775 (2019) 1164–1176.
- [27] Y. Li, Y. Ding, K. Munir, J. Lin, M. Brandt, A. Atrens, Y. Xiao, J.R. Kanwar, C. Wen, Novel β -Ti35Zr28Nb alloy scaffolds manufactured using selective laser melting for bone implant applications, *Acta Biomater.* 87 (2019) 273–284.
- [28] J.P. Luo, J.F. Sun, Y.J. Huang, J.H. Zhang, Y.D. Zhang, D.P. Zhao, M. Yan, Low-modulus biomedical Ti-30Nb-5Ta-3Zr additively manufactured by Selective Laser Melting and its biocompatibility, *Mater. Sci. Eng. C* 97 (2019) 275–284.
- [29] L.C. Zhang, D. Klemm, J. Eckert, Y.L. Hao, T.B. Sercombe, Manufacture by selective laser melting and mechanical behavior of a biomedical Ti-24Nb-4Zr-8Sn alloy, *Scripta Mater.* 65 (1) (2011) 21–24.
- [30] Y.J. Liu, H.L. Wang, S.J. Li, S.G. Wang, W.J. Wang, W.T. Hou, Y.L. Hao, R. Yang, L. C. Zhang, Compressive and fatigue behavior of beta-type titanium porous structures fabricated by electron beam melting, *Acta Mater.* 126 (2017) 58–66.
- [31] Y.-L. Zhou, M. Niinomi, Ti-25Ta alloy with the best mechanical compatibility in Ti-Ta alloys for biomedical applications, *Mater. Sci. Eng. C* 29 (3) (2009) 1061–1065.
- [32] R. Wauthle, J. van der Stok, S. Amin Yavari, J. Van Humbeeck, J.-P. Kruth, A. A. Zadpoor, H. Weinans, M. Mulier, J. Schrooten, Additively manufactured porous tantalum implants, *Acta Biomater.* 14 (2015) 217–225.
- [33] Y. Zhu, Y. Gu, S. Qiao, L. Zhou, J. Shi, H. Lai, Bacterial and mammalian cells adhesion to tantalum-decorated micro-/nano-structured titanium, *J. Biomed. Mater. Res.* 105 (3) (2017) 871–878.
- [34] J. Tae-Sik, J. Hyun-Do, K. Sungwon, M. Byeong-Seok, B. Jaeuk, P. Cheonil, S. Juha, K. Hyoun-Ee, Multiscale porous titanium surfaces via a two-step etching process for improved mechanical and biological performance, *Biomed. Mater.* 12 (2) (2017), 025008.
- [35] E.G. Brodie, A.E. Medvedev, J.E. Frith, M.S. Dargusch, H.L. Fraser, A. Molotnikov, Remelt processing and microstructure of selective laser melted Ti25Ta, *J. Alloys Compd.* 820 (2020), 153082.
- [36] N. Soro, H. Attar, E. Brodie, M. Veidt, A. Molotnikov, M.S. Dargusch, Evaluation of the mechanical compatibility of additively manufactured porous Ti-25Ta alloy for load-bearing implant applications, *J. Mech. Behav. Biomed.* 97 (2019) 149–158.
- [37] S. Ghouse, S. Babu, K. Nai, P.A. Hooper, J.R.T. Jeffers, The influence of laser parameters, scanning strategies and material on the fatigue strength of a stochastic porous structure, *Addit. Manuf.* 22 (2018) 290–301.
- [38] R. Wauthle, S.M. Ahmadi, S. Amin Yavari, M. Mulier, A.A. Zadpoor, H. Weinans, J. Van Humbeeck, J.-P. Kruth, J. Schrooten, Revival of pure titanium for dynamically loaded porous implants using additive manufacturing, *Mater. Sci. Eng. C* 54 (C) (2015) 94–100.
- [39] K.A. Bywater, J.W. Christian, Martensitic transformations in titanium-tantalum alloys, *The Philosophical Magazine: A Journal of Theoretical Experimental and Applied Physics* 25 (6) (1972) 1249–1273.
- [40] C.-M. Wu, P.-W. Peng, H.-H. Chou, K.-L. Ou, E. Sugiatno, C.-M. Liu, C.-F. Huang, Microstructural, mechanical and biological characterizations of the promising titanium-tantalum alloy for biomedical applications, *J. Alloys Compd.* 735 (2018) 2604–2610.
- [41] S. Huang, S.L. Sing, G. Delooze, R. Wilson, W.Y. Yeong, Laser powder bed fusion of titanium-tantalum alloys: compositions and designs for biomedical applications, *J. Mech. Behav. Biomed.* (2020), 103775.
- [42] A.V. Dobromyslov, G.V. Dolgikh, Y. Dutkovich, T.L. Trenogina, Phase and structural transformations in Ti-Ta alloys, *Phys. Met. Metallogr.* 107 (5) (2009) 502–510.
- [43] K. Majchrowicz, Z. Pakiela, T. Brynk, B. Romelczyk-Baishya, M. Płocińska, T. Kurzynowski, E. Chlebus, Microstructure and mechanical properties of Ti-Re alloys manufactured by selective laser melting, *Mater. Sci. Eng., A* 765 (2019), 138290.
- [44] R. Martinez, I. Todd, K. Mumtaz, In situ alloying of elemental Al-Cu12 feedstock using selective laser melting, *Virtual Phys. Prototyp.* 14 (3) (2019) 242–252.
- [45] Z. Xiao, C. Chen, Z. Hu, H. Zhu, X. Zeng, Effect of rescanning cycles on the characteristics of selective laser melting of Ti6Al4V, *Opt. Laser Tehcnol.* 122 (2020), 105890.
- [46] C.L.A. Leung, S. Marussi, M. Towrie, R.C. Atwood, P.J. Withers, P.D. Lee, The effect of powder oxidation on defect formation in laser additive manufacturing, *Acta Mater.* 166 (2019) 294–305.
- [47] B. Liu, B.-Q. Li, Z. Li, Selective laser remelting of an additive layer manufacturing process on AlSi10Mg, *Results Phys.* 12 (2019) 982–988.
- [48] W. Yu, S.L. Sing, C.K. Chua, X. Tian, Influence of re-melting on surface roughness and porosity of AlSi10Mg parts fabricated by selective laser melting, *J. Alloys Compd.* 792 (2019) 574–581.
- [49] E. Yasa, J.P. Kruth, Microstructural investigation of Selective Laser Melting 316L stainless steel parts exposed to laser re-melting, *Procedia Eng.* 19 (2011) 389–395.
- [50] Y. Yao, X. Li, Y.Y. Wang, W. Zhao, G. Li, R.P. Liu, Microstructural evolution and mechanical properties of Ti-Zr beta titanium alloy after laser surface remelting, *J. Alloys Compd.* 583 (2014) 43–47.
- [51] J. Vaithilingam, R.D. Goodridge, R.J.M. Hague, S.D.R. Christie, S. Edmondson, The effect of laser remelting on the surface chemistry of Ti6Al4V components fabricated by selective laser melting, *J. Mater. Process. Technol.* 232 (2016) 1–8.
- [52] T. Gustmann, H. Schwab, U. Kühn, S. Pauly, Selective laser remelting of an additively manufactured Cu-Al-Ni-Mn shape-memory alloy, *Mater. Des.* 153 (2018) 129–138.
- [53] S. Griffiths, M.D. Rossell, J. Croteau, N.Q. Vo, D.C. Dunand, C. Leinenbach, Effect of laser rescanning on the grain microstructure of a selective laser melted Al-Mg-Zr alloy, *Mater. Char.* 143 (2018) 34–42.
- [54] K. Wei, M. Lv, X. Zeng, Z. Xiao, G. Huang, M. Liu, J. Deng, Effect of laser remelting on deposition quality, residual stress, microstructure, and mechanical property of selective laser melting processed Ti-5Al-2.5Sn alloy, *Mater. Char.* 150 (2019) 67–77.
- [55] Z. Xiong, P. Zhang, C. Tan, D. Dong, W. Ma, K. Yu, Selective laser melting and remelting of pure tungsten, *Adv. Eng. Mater.* 22 (3) (2020), 1901352.
- [56] J. Guan, Y. Jiang, X. Zhang, X. Chong, Microstructural evolution and EBSD analysis of AlSi10Mg alloy fabricated by selective laser remelting, *Mater. Char.* 161 (2020), 110079.
- [57] B. AlMangour, D. Grzesiak, J.-M. Yang, Scanning strategies for texture and anisotropy tailoring during selective laser melting of TiC/316L stainless steel nanocomposites, *J. Alloys Compd.* 728 (2017) 424–435.
- [58] W. Weng, A. Biesiekierski, Y. Li, C. Wen, Effects of selected metallic and interstitial elements on the microstructure and mechanical properties of beta titanium alloys for orthopedic applications, *Materialia* 6 (2019), 100323.
- [59] A. Ramarolahy, P. Castany, F. Prima, P. Laheurte, I. Péron, T. Gloriant, Microstructure and mechanical behavior of superelastic Ti-24Nb-0.50 biomedical alloys, *J. Mech. Behav. Biomed.* 9 (2012) 83–90.
- [60] Y.B. Wang, Y.F. Zheng, The microstructure and shape memory effect of Ti-16 at.% Nb alloy, *Mater. Lett.* 62 (2) (2008) 269–272.
- [61] Y.L. Zhou, M. Niinomi, T. Akahori, Effects of Ta content on Young's modulus and tensile properties of binary Ti-Ta alloys for biomedical applications, *Mater. Sci. Eng., A* 371 (1–2) (2004) 283–290.
- [62] S. Huang, S.L. Sing, W.Y. Yeong, Selective laser melting of Ti42Nb composite powder and the effect of laser Re-melting, *Key Eng. Mater.* 801 (2019) 270–275.
- [63] H. Schwab, G.K. Prashanth, L. Löber, U. Kühn, J. Eckert, Selective laser melting of Ti-45Nb alloy, *Metals* 5 (2) (2015) 686–694.
- [64] C. Schulze, M. Weinmann, C. Schweigeler, O. Kefler, R. Bader, Mechanical properties of a newly additive manufactured implant material based on Ti-42Nb, *Materials* 11 (1) (2018) 124.
- [65] M. Fischer, D. Jouquet, G. Robin, L. Peltier, P. Laheurte, In situ elaboration of a binary Ti-26Nb alloy by selective laser melting of elemental titanium and niobium mixed powders, *Mater. Sci. Eng. C* 62 (2016) 852–859.
- [66] M. Speirs, J.V. Humbeeck, J. Schrooten, J. Luyten, J.P. Kruth, The effect of pore geometry on the mechanical properties of selective laser melted Ti-13Nb-13Zr scaffolds, *Procedia CIRP* 5 (2013) 79–82.
- [67] N. Hafeez, S. Liu, E. Lu, L. Wang, R. Liu, W. Lu, L.-C. Zhang, Mechanical behavior and phase transformation of β -type Ti-35Nb-2Ta-3Zr alloy fabricated by 3D-Printing, *J. Alloys Compd.* 790 (2019) 117–126.
- [68] J. Hernandez, S.J. Li, E. Martinez, L.E. Murr, X.M. Pan, K.N. Amato, X.Y. Cheng, F. Yang, C.A. Terrazas, S.M. Gaytan, Y.L. Hao, R. Yang, F. Medina, R.B. Wicker, Microstructures and hardness properties for β -phase Ti-24Nb-4Zr-7.9Sn alloy fabricated by electron beam melting, *J. Mater. Sci. Technol.* 29 (11) (2013) 1011–1017.
- [69] S.L. Sing, W.Y. Yeong, F.E. Wiria, Selective laser melting of titanium alloy with 50 wt% tantalum: microstructure and mechanical properties, *J. Alloys Compd.* 660 (2016) 461–470.
- [70] D. Zhao, C. Han, Y. Li, J. Li, K. Zhou, Q. Wei, J. Liu, Y. Shi, Improvement on mechanical properties and corrosion resistance of titanium-tantalum alloys in-situ fabricated via selective laser melting, *J. Alloys Compd.* 804 (2019) 288–298.
- [71] P. Li, D.H. Warner, A. Fatemi, N. Phan, Critical assessment of the fatigue performance of additively manufactured Ti-6Al-4V and perspective for future research, *Int. J. Fatig.* 85 (2016) 130–143.
- [72] I.J. Beyerlein, L.S. Tóth, Texture evolution in equal-channel angular extrusion, *Prog. Mater. Sci.* 54 (4) (2009) 427–510.
- [73] H. Matsumoto, H. Yoneda, K. Sato, S. Kurosu, E. Maire, D. Fabregue, T.J. Konno, A. Chiba, Room-temperature ductility of Ti-6Al-4V alloy with α' martensite microstructure, *Mater. Sci. Eng., A* 528 (3) (2011) 1512–1520.
- [74] T. Niendorf, P. Krooß, E. Batyrsina, A. Paulsen, Y. Motemani, A. Ludwig, P. Buenconsejo, J. Frenzel, G. Eggeler, H.J. Maier, Functional and structural fatigue of titanium tantalum high temperature shape memory alloys (HT SMAs), *Mater. Sci. Eng., A* 620 (2015) 359–366.
- [75] G. Chen, J. Yin, S. Zhao, H. Tang, X. Qu, Microstructure and tensile properties of a Ti-28Ta alloy studied by transmission electron microscopy and digital image correlation, *Int. J. Refract. Metals Hard Mater.* 81 (2019) 71–77.

- [76] Y.-L. Zhou, M. Niinomi, T. Akahori, M. Nakai, H. Fukui, Comparison of various properties between titanium-tantalum alloy and pure titanium for biomedical applications, *Mater. Trans.* 48 (3) (2007) 380–384.
- [77] B. Wysocki, P. Maj, A. Krawczyńska, K. Rożniatowski, J. Zdunek, K. J. Kurzydłowski, W. Święszkowski, Microstructure and mechanical properties investigation of CP titanium processed by selective laser melting (SLM), *J. Mater. Process. Technol.* 241 (2017) 13–23.
- [78] J. Haubrich, J. Gussone, P. Barriobero-Vila, P. Kürnsteiner, E.A. Jägle, D. Raabe, N. Schell, G. Requena, The role of lattice defects, element partitioning and intrinsic heat effects on the microstructure in selective laser melted Ti-6Al-4V, *Acta Mater.* 167 (2019) 136–148.
- [79] B. Wysocki, J. Idaszek, J. Zdunek, K. Rożniatowski, M. Pisarek, A. Yamamoto, W. Święszkowski, The influence of selective laser melting (SLM) process parameters on in-vitro cell response, *Int. J. Mol. Sci.* 19 (6) (2018) 1619.
- [80] L. Thijss, F. Verhaeghe, T. Craeghs, J.V. Humbeeck, J.-P. Kruth, A study of the microstructural evolution during selective laser melting of Ti-6Al-4V, *Acta Mater.* 58 (9) (2010) 3303–3312.
- [81] A.G. Demir, B. Previtali, Investigation of remelting and preheating in SLM of 18Ni300 maraging steel as corrective and preventive measures for porosity reduction, *Int. J. Adv. Manuf. Technol.* 93 (5) (2017) 2697–2709.
- [82] H. Ali, H. Ghadbeigi, K. Mumtaz, Effect of scanning strategies on residual stress and mechanical properties of Selective Laser Melted Ti6Al4V, *Mater. Sci. Eng., A* 712 (2018) 175–187.
- [83] CES EduPack, Granta Design Limited, 2019.
- [84] H. Mughrabi, Microstructural mechanisms of cyclic deformation, fatigue crack initiation and early crack growth, *Philos. Trans. Royal Soc. A* 373 (2015), 20140132, 2038.
- [85] S. Romano, A. Abel, J. Gumpinger, A.D. Brandão, S. Beretta, Quality control of AlSi10Mg produced by SLM: metallography versus CT scans for critical defect size assessment, *Addit. Manuf.* 28 (2019) 394–405.
- [86] S. Romano, S. Miccoli, S. Beretta, A new FE post-processor for probabilistic fatigue assessment in the presence of defects and its application to AM parts, *Int. J. Fatig.* 125 (2019) 324–341.
- [87] P. Bleys, J.P. Kruth, B. Lauwers, B. Schacht, V. Balasubramanian, L. Froyen, J. Van Humbeeck, Surface and sub-surface quality of steel after EDM, *Adv. Eng. Mater.* 8 (1-2) (2006) 15–25.
- [88] C. Shoba, N. Ramaiah, D.N. Rao, Influence of dislocation density on the residual stresses induced while machining Al/SiC/RHA hybrid composites, *J. Mater. Res. Technol.* 4 (3) (2015) 273–277.
- [89] A. Baczmanski, K. Wierzanowski, P. Lipinski, B. Bacroix, A. Lodini, Residual stresses, dislocation density and recrystallization process, *J. Neutron Res.* 15 (2007) 281–287.
- [90] S. Amin Yavari, R. Wauthle, J. van der Stok, A.C. Riemsdag, M. Janssen, M. Mulier, J.P. Kruth, J. Schrooten, H. Weinans, A.A. Zadpoor, Fatigue behavior of porous biomaterials manufactured using selective laser melting, *Mater. Sci. Eng. C* 33 (8) (2013) 4849–4858.
- [91] M. Kiyak, O. Çakır, Examination of machining parameters on surface roughness in EDM of tool steel, *J. Mater. Process. Technol.* 191 (1) (2007) 141–144.
- [92] Y. Keskin, H.S. Halkaci, M. Kizil, An experimental study for determination of the effects of machining parameters on surface roughness in electrical discharge machining (EDM), *Int. J. Adv. Manuf. Technol.* 28 (11) (2006) 1118–1121.
- [93] J.Y. Kao, C.C. Tsao, S.S. Wang, C.Y. Hsu, Optimization of the EDM parameters on machining Ti-6Al-4V with multiple quality characteristics, *Int. J. Adv. Manuf. Technol.* 47 (1) (2010) 395–402.
- [94] A. Hasçalık, U. Çaydaş, Electrical discharge machining of titanium alloy (Ti-6Al-4V), *Appl. Surf. Sci.* 253 (22) (2007) 9007–9016.
- [95] L. Zhang, G. Yang, B.N. Johnson, X. Jia, Three-dimensional (3D) printed scaffold and material selection for bone repair, *Acta Biomater.* 84 (2019) 16–33.
- [96] A.A. Zadpoor, Mechanical performance of additively manufactured meta-biomaterials, *Acta Biomater.* 85 (2019) 41–59.
- [97] E. Alabot, D. Barba, R.C. Reed, Design of metallic bone by additive manufacturing, *Scripta Mater.* 164 (2019) 110–114.